sample burning in 21% oxygen is shown in Fig. 2. The flame burns the length of the sample in 11 s. The camera detects small glowing pieces shooting out from the flame and some of the char glowing and folding over into the flame. The width of the flame on each side of the paper changes during the burn. During this time, the lateral g level crosses from one direction to the other. The 18% oxygen, laboratory wiper flame, not shown here, burns to completion in the reduced-gravity period. The intensified array camera gains for these two flames are 72 and 1800. The flames would have been difficult to detect using film or conventional color CCD cameras. An additional test using 18% oxygen, with the narrowband interference filter, produced inconclusive results. Because the filter bandwidth of 1 nm is too narrow compared to the CH spectral bandwidth of 10–15 nm at flame temperatures, the image appears dim. The laboratory wiper sample in 15% oxygen appear to ignite but extinguishes quickly. No flame is detected after 5 s with the camera at its highest gain.

Flame Spread Rates

Measurements of the flame spread rates are useful for an order-of-magnitude comparison to other reduced-gravity measurements, although the induced flows due to buoyancy are not known. For each flame, the leading edge is specified to occur at a gray level chosen by eye, e.g., 60 out of 255, and its position is measured for each frame. The relative flame positions vs time from ignition for four tests are shown in Fig. 3. After the first few seconds of ignition and stabilization, the flames spread steadily over the paper samples.

The average flame spread rates for the ashless filter paper burning in 21% oxygen and 18% oxygen are 0.16 cm/s and 0.09 cm/s, respectively. The approximate z-axis g level for the 18% oxygen test oscillates between ± 0.02 g. The flame position advances and retreats on a timescale of seconds and appears to correlate, as does the flame standoff, with positive and negative g levels. As the flame advances, the leading edge narrows and approaches the paper; as the flame retreats, the leading edge widens. Both flames move little during the reduced-gravity time and may be influenced by the presence of the ignitor. There is little data obtained in reduced gravity for this fuel with which to make a comparison. Some unpublished data, obtained in the NASA Lewis Zero Gravity facility, show that ashless filter paper samples burning in a 1 atm, 30% oxygen–70% nitrogen, quiescent environment have a spread rate of approximately 0.12 cm/s.[6] The flame images are dim blue and difficult to analyze. The flame spread rate observed here for ashless filter paper in 21% oxygen is higher than that measured in the quiescent, 30% oxygen drop tower test, probably due to the induced buoyant flow from the residual g level.

The laboratory wiper samples burn faster than the ashless filter paper samples. The average flame spread rates for the laboratory wiper in 21% oxygen and 18% oxygen are 0.8 cm/s and 0.5 cm/s, respectively. Previous drop tower experiments using this fuel show a spread rate of 0.54 cm/s at the molar oxygen extinction limit of 21% for quiescent flame spread.[2] When a slow opposed flow or concurrent flow on the order of 5–7 cm/s is imposed, the flame spread rate increases above the quiescent flame spread rate.[2,3] The flame spread rate for the laboratory wiper in 21% oxygen observed here is higher than the quiescent drop tower measurement, but is consistent with the presence of induced flows on the order of those studied in the forced-flow experiments in the drop tower. Likewise, the flame spread rate for a laboratory wiper in 18% oxygen observed here is similar to those measured using a slow opposed flow or concurrent flow in the drop tower.[2,3]

Conclusions

An intensified array camera has successfully imaged weakly luminous flames spreading over thermally thin paper samples in a reduced-gravity environment aboard the NASA Learjet. The residual g level of the aircraft affects the flammability, flame shapes, and spread rates. The flammability and measured flame spread rates for the laboratory wipers in 21 and 18% oxygen for these "quiescent" aircraft experiments are similar to those obtained in forced-flow drop tower experiments, suggesting substantial induced flows due to the residual g levels are present.

References

[1]The Microgravity Combustion Group, "Microgravity Combustion Science: Progress, Plans, and Opportunities," NASA TM-105410, April 1992, pp. 6–11.

[2]Olson, S. L., Ferkul, P. V., and T'ien, J. S., "Near-limit Flame Spread over a Thin Solid Fuel in Microgravity," *Twenty-Second Symposium (International) on Combustion,* Combustion Inst., Pittsburgh, PA, 1988, pp. 1213–1222.

[3]Grayson, G., Sacksteder, K. R., and T'ien, J. S., "An Experimental Study of Low-Speed, Concurrent-Flow Flame Spread over a Thin Fuel," Central States Meeting of the Combustion Inst., Nashville, TN, 1991.

[4]Vento, D. M., Zavesky, R. J., Sacksteder, K. R., and Altenkirch, R. A., "The Solid Surface Combustion Space Shuttle Experiment Hardware Description and Ground-Based Test Results," AIAA Paper 89-0503, Jan. 1989; also NASA TM-101963.

[5]Weiland, K. J., "Intensified Array Camera Imaging of Solid Surface Combustion Aboard the NASA Learjet," AIAA Paper 92-0240, Jan. 1992; also NASA TM-105361, 1992.

[6]Olson, S. L., private communication, NASA Lewis Research Center, Cleveland, OH, Nov. 1991.

Implicit Treatment of Diffusion Terms in Lower-Upper Algorithms

T. I-P. Shih* and E. Steinthorsson†
Carnegie Mellon University,
Pittsburgh, Pennsylvania 15213
and
W. J. Chyu‡
NASA Ames Research Center,
Moffett Field, California 94035

Introduction

THE lower-upper (LU) algorithm[1,2] is a highly efficient method for obtaining numerical solutions to the "compressible" Euler and Navier-Stokes (N-S) equations. So far, when using the LU algorithm to analyze the N-S equations, the diffusion terms have usually been treated explicitly.[3–6] This is because the LU algorithm factors according to the signs of eigenvalues associated with the Jacobians of the flux vectors, and such eigenvalues do not exist for the diffusion terms. When diffusion terms are treated explicitly, the robustness of the LU algorithm can be degraded. In fact for three-dimensional problems, numerical experiments have indicated that the LU algorithm can become unconditionally unstable if the residual is dominated by diffusion terms.[6]

In this Technical Note, a method is presented which allows diffusion terms to be treated implicitly in the LU algorithm in order that its good stability properties will not be impaired. The method presented generalizes the concept of LU factorization from that associated with the signs of eigenvalues to that associated with backward- and forward-difference operators without regard to eigenvalues.

Received May 11, 1992; revision received Oct. 13, 1992; accepted for publication Oct. 16, 1992.

*Associate Professor, Department of Mechanical Engineering. Member AIAA.

†Graduate Student, Department of Mechanical Engineering. Member AIAA.

‡Research Scientist, Applied Aerodynamics Branch. Member AIAA.

Methodology

To illustrate the method for treating diffusion terms implicitly, consider the following model equation:

$$\frac{\partial u}{\partial t} + c_x \frac{\partial u}{\partial x} + c_y \frac{\partial u}{\partial y} = \mu \left(\frac{\partial^2 u}{\partial x^2} + \frac{\partial^2 u}{\partial y^2} \right) \tag{1}$$

where u is the dependent variable, and c_x, c_y, and μ are constants. Suppose that the domain for Eq. (1) is discretized so that the time-step size (Δt) and grid spacings (Δx and Δy) are all constants.

By using the Euler implicit time-differencing formula for the time derivative, upwind differencing for the convection terms, and central differencing for the diffusion terms, Eq. (1) can be written in the following delta form:

$$\left[1 + \sum_{s=x,y} (a_s^+ \delta_s^f + a_s^- \delta_s^f - b_s \delta_s^2) \right] \Delta u_{i,j}^{n+1} = \text{RHS} \tag{2a}$$

where

$$\text{RHS} = - \sum_{s=x,y} (a_s^+ \delta_s^b + a_s^- \delta_s^f - b_s \delta_s^2)\, u_{i,j}^n \tag{2b}$$

In Eqs. (2), $a^{\pm} = (a \pm |a|)/2$; $a_s = c_s \Delta t/\Delta s$; $b_s = \mu \Delta t/\Delta s^2$; δ^b, δ^f, and δ are backward-, forward-, and central-difference operators, respectively; and $\Delta u^{n+1} = u^{n+1} - u^n$.

Since $\delta^2 = \delta^f - \delta^b$, Eq. (2a) can be rearranged in terms of backward- and forward-difference to give

$$[1 + (B^+ + B^-)]\, \Delta u_{i,j}^{n+1} = (1 + B^+)(1 + B^-)\, \Delta u_{i,j}^{n+1} = \text{RHS} \tag{3a}$$

where

$$B^{+,-} = \sum_{s=x,y} (a_s^{+,-} \pm b_s)\, \delta_s^{b,f} \tag{3b}$$

and which can be split as

$$(1 + B^+)\, \Delta u_{i,j}^* = \text{RHS} \tag{4a}$$

$$(1 + B^-)\, \Delta u_{i,j}^{n+1} = \Delta u_{i,j}^* \tag{4b}$$

Application of Eq. (4a) at every grid point or cell produces a lower triangular matrix. In a similar manner, Eq. (4b) produces an upper triangular matrix.

From Eqs. (3b) and (4), it can be seen that the method of LU factorization presented here allows both the convection and the diffusion terms to be treated implicitly.

Stability Analysis

In this section, we show that the method presented in the previous section is unconditionally stable. To simplify analysis, let all y derivatives in Eq. (1) equal to zero and $c_x > 0$ so that $a_x^- = 0$ and $a_x^+ = a_x$. With these simplifications and noting that $\delta^2 = \delta^f - \delta^b$ and $\delta^b \delta^f()_i = \delta^f()_i - \delta^f()_{i-1} = \delta^2()_i$, Eq. (4) can be written as

$$\begin{aligned} &(1 + a_x \delta_x^b + b_x \delta_x^b)\, (1 - b_x \delta_x^f)\, \Delta u_i^{n+1} \\ &= [1 + a_x \delta_x^b - (b_x + a_x b_x + b_x^2)\, \delta_x^2]\, \Delta u_i^{n+1} \\ &= -(a_x \delta_x^b - b_x \delta_x^2)\, u_i^n \end{aligned} \tag{5}$$

By using the Fourier method of stability analysis, we obtain the following amplification factor for Eq. (5):

$$|G|^2 = \frac{[1 + 2(a_x b_x + b_x^2)\,(1 - \cos\phi)]^2}{[1 + 2(a_x/2 + b_x + a_x b_x + b_x^2)\,(1 - \cos\phi)]^2 + a_x^2 \sin^2\phi} \tag{6}$$

where $G = A^{n+1}/A^n$; $\phi = k\Delta x$; and A and k are the amplitude and the wave number of a Fourier component, respectively. Since a_x and b_x are both positive, it can be seen from Eq. (6) that the absolute value of G is less than or equal to unity for all wave numbers k—indicating unconditional stability.

If the diffusion term is treated explicitly [i.e., $b_x = 0$ only on the two left-hand sides of Eq. (5)], then the amplification factor of the resulting equation is given by

$$|G|^2 = \frac{[1 - 2b_x(1 - \cos\phi)]^2}{1 + 2a_x(1 + a_x)\,(1 - \cos\phi)} \tag{7}$$

From Eq. (7), it can be seen that if b_x is sufficiently large, then the absolute value of G can exceed unity—indicating conditional stability.

Application to the k-ε Model of Turbulence

To demonstrate the usefulness of the method presented in this study, it was applied to the k-ε model of Chen and Patel[7] to simulate the turbulence properties in a turbulent boundary layer. The k-ε model of Chen and Patel divides the turbulent flowfield into two regions. One region—referred to as the wall region—extends from the wall to the edge of the fully turbulent region. The other region—referred to as the core region—contains the rest of the turbulent flowfield which is fully turbulent everywhere. In the wall region, the one-equation model of Wolfshtein[8] is used, and in the core region, the standard k-ε model is used.

The standard k-ε model involves two partial differential equations and can be written in the following vector form:

$$\frac{\partial \boldsymbol{U}}{\partial t} + \frac{\partial \boldsymbol{E}}{\partial x} + \frac{\partial \boldsymbol{F}}{\partial y} + \frac{\partial \boldsymbol{G}}{\partial z} + \boldsymbol{H} = \frac{\partial \boldsymbol{R}}{\partial x} + \frac{\partial \boldsymbol{S}}{\partial y} + \frac{\partial \boldsymbol{T}}{\partial z} \tag{8}$$

where

$$\boldsymbol{U} = \begin{bmatrix} \rho k \\ \rho \varepsilon \end{bmatrix} \quad \boldsymbol{H} = \begin{bmatrix} -(G - \rho\varepsilon) \\ -S \end{bmatrix} \quad \boldsymbol{R} = \begin{bmatrix} \left(\mu + \dfrac{\mu_t}{\sigma_k}\right)\dfrac{\partial k}{\partial x} \\ \left(\mu + \dfrac{\mu_t}{\sigma_\varepsilon}\right)\dfrac{\partial \varepsilon}{\partial x} \end{bmatrix}$$

$$\boldsymbol{S} = \begin{bmatrix} \left(\mu + \dfrac{\mu_t}{\sigma_k}\right)\dfrac{\partial k}{\partial y} \\ \left(\mu + \dfrac{\mu_t}{\sigma_\varepsilon}\right)\dfrac{\partial \varepsilon}{\partial y} \end{bmatrix} \quad \boldsymbol{T} = \begin{bmatrix} \left(\mu + \dfrac{\mu_t}{\sigma_k}\right)\dfrac{\partial k}{\partial z} \\ \left(\mu + \dfrac{\mu_t}{\sigma_\varepsilon}\right)\dfrac{\partial \varepsilon}{\partial z} \end{bmatrix} \tag{9}$$

$$\begin{aligned} G = \mu_t \Bigg[&2\left(\frac{\partial u}{\partial x}\right)^2 + 2\left(\frac{\partial v}{\partial y}\right)^2 + 2\left(\frac{\partial w}{\partial z}\right)^2 \\ &+ \left(\frac{\partial v}{\partial x} + \frac{\partial u}{\partial y}\right)^2 + \left(\frac{\partial w}{\partial y} + \frac{\partial v}{\partial z}\right)^2 + \left(\frac{\partial u}{\partial z} + \frac{\partial w}{\partial x}\right)^2 \Bigg] \\ &- \frac{2}{3}(\nabla \cdot \boldsymbol{V})\,[\mu_t(\nabla \cdot \boldsymbol{V}) + \rho k] \end{aligned} \tag{10}$$

In the preceding equations, k is the turbulent kinetic energy, ε the dissipation rate of k, ρ the Favre-averaged density; u, v, and w are the x, y, and z components of the Favre-averaged velocity vector $\boldsymbol{V}$; μ is the dynamic viscosity; $\mu_t = C_\mu \rho k^2/\varepsilon$; $C_\mu = 0.09$; $C_1 = 1.44$; $C_2 = 1.92$; $\sigma_k = 1.0$; $\sigma_\varepsilon = 1.3$; $\boldsymbol{E} = u\boldsymbol{U}$; $\boldsymbol{F} = v\boldsymbol{U}$; $\boldsymbol{G} = w\boldsymbol{U}$; and $S = C_1 G(\varepsilon/k) - C_2 \rho(\varepsilon^2/k)$.

The one-equation model of Wolfshtein uses the first equation in the vector equation given by Eq. (8) to calculate k. The ε and μ_t are calculated by the following algebraic equation: $\varepsilon = k^{3/2}/L_\varepsilon$ and $\mu_t = C_\mu \rho k^{1/2} L_\mu$, where $L_\varepsilon = C_L \hat{y}\ [1 - \exp(-R_{\hat{y}}/A_\varepsilon)]$, $L_\mu = C_L \hat{y}\ [1 - \exp(-R_{\hat{y}}/A_\mu)]$, $C_L = k/C_\mu^{3/4}$, $A_\varepsilon = 2C_L$ (chosen so that $\varepsilon = 2\mu k/\rho \hat{y}^2$ in the linear sublayer), $A_\mu = 70$ (chosen so that the additive constant in the law of the wall is recovered); $R_{\hat{y}} = \rho k^{1/2} \hat{y}/\mu$, and $\hat{y}$ is the normal distance from the wall. Numerical experiments show that the $\hat{y}$ coordinate separating the wall and core regions must be such that $R_{\hat{y}}$ is greater than 200.

If the k-ε model just described can be lagged behind the conservation equations of mass, momentum, and energy by one timestep in the solution procedure, then ρ, u, v, w, and μ are known, and only k and ε are unknown. By adopting this approach and by using generalized coordinates [i.e., mapping (x, y, z, t) to (ξ, η, ζ, τ) for arbitrary geometries], Eq. (8) can be written as

$$\frac{\partial \boldsymbol{U}J}{\partial \tau}+\frac{\partial \hat{\boldsymbol{E}}}{\partial \xi}+\frac{\partial \hat{\boldsymbol{F}}}{\partial \eta}+\frac{\partial \hat{\boldsymbol{G}}}{\partial \zeta}+\boldsymbol{H}J=\frac{\partial \hat{\boldsymbol{R}}}{\partial \xi}+\frac{\partial \hat{\boldsymbol{S}}}{\partial \eta}+\frac{\partial \hat{\boldsymbol{T}}}{\partial \zeta} \tag{11}$$

In Eq. (11), $J=\partial(x, y, z, t)/\partial(\xi, \eta, \zeta, \tau)$ is the Jacobian; $\hat{\boldsymbol{E}}=\hat{U}\boldsymbol{U}$; $\hat{\boldsymbol{F}}=\hat{V}\boldsymbol{U}$; $\hat{\boldsymbol{G}}=\hat{W}\boldsymbol{U}$; $\hat{\boldsymbol{R}}=\hat{\xi}_x\boldsymbol{R}+\hat{\xi}_y\boldsymbol{S}+\hat{\xi}_z\boldsymbol{T}$; $\hat{U}=\hat{\xi}_t+u\hat{\xi}_x+v\hat{\xi}_y+w\hat{\xi}_z$; $\boldsymbol{A}_\xi=J\nabla\xi=J(\xi_x\boldsymbol{i}+\xi_y\boldsymbol{j}+\xi_z\boldsymbol{k})=\hat{\xi}_x\boldsymbol{i}+\hat{\xi}_y\boldsymbol{j}+\hat{\xi}_z\boldsymbol{k}$; and similarly for $\hat{\boldsymbol{S}}, \hat{\boldsymbol{T}}, \hat{V}, \hat{W}$, $\boldsymbol{A}_\eta$, and $\boldsymbol{A}_\zeta$.

By using the Euler implicit time-differencing formula (or a higher-order accurate formula if transient solutions are of interest) and linearizing nonlinear terms, Eq. (11) becomes

$$\left\{J^{n+1}\boldsymbol{I}+\Delta t\left[\frac{\partial}{\partial \xi}\hat{U}^{n+1}\boldsymbol{I}+\frac{\partial}{\partial \eta}\hat{V}^{n+1}\boldsymbol{I}+\frac{\partial}{\partial \zeta}\hat{W}^{n+1}\boldsymbol{I}+\boldsymbol{D}-\sum_{\sigma=\xi,\eta,\zeta}\frac{\partial}{\partial \sigma}\boldsymbol{A}_{\sigma\sigma}\frac{\partial}{\partial \sigma}\frac{\boldsymbol{I}}{\rho^{n+1}}\right]\right\}\Delta\boldsymbol{U}^{n+1}=\text{RHS} \tag{12a}$$

where

$$\text{RHS}=\Delta t\left\{-\frac{\partial}{\partial \xi}\hat{U}^{n+1}\boldsymbol{U}^n-\frac{\partial}{\partial \eta}\hat{V}^{n+1}\boldsymbol{U}^n-\frac{\partial}{\partial \zeta}\hat{W}^{n+1}\boldsymbol{U}^n-J^{n+1}\boldsymbol{H}^n+\sum_{\sigma=\xi,\eta,\zeta}\frac{\partial}{\partial \sigma}\boldsymbol{A}_{\sigma\sigma}\frac{\partial}{\partial \sigma}\frac{\boldsymbol{U}^n}{\rho^{n+1}}\right\}-\boldsymbol{U}^n\Delta J^{n+1} \tag{12b}$$

$$\boldsymbol{A}_{\xi\eta}=\boldsymbol{A}_{\eta\xi}=\begin{bmatrix}\left(\mu+\dfrac{\mu_t}{\sigma_k}\right)M_{\xi\eta} & 0\\ 0 & \left(\mu+\dfrac{\mu_t}{\sigma_\varepsilon}\right)M_{\xi\eta}\end{bmatrix}$$

$$M_{\xi\eta}=M_{\eta\xi}=\frac{(\hat{\xi}_x\hat{\eta}_x+\hat{\xi}_y\hat{\eta}_y+\hat{\xi}_z\hat{\eta}_z)^{n+1}}{J^{n+1}} \tag{12c}$$

In Eqs. (12), n and $n+1$ denote the nth and $(n+1)$th time levels, respectively; $\Delta\boldsymbol{U}^{n+1}=\boldsymbol{U}^{n+1}-\boldsymbol{U}^n$; $\Delta J^{n+1}=J^{n+1}-J^n$; $\boldsymbol{D}=J^{n+1}(\partial \boldsymbol{G}/\partial \boldsymbol{U})^n$; and $\boldsymbol{I}$ is a 2×2 identity matrix. $\boldsymbol{A}_{\xi\xi}$, $\boldsymbol{A}_{\xi\zeta}$, $\boldsymbol{A}_{\eta\eta}$, . . . , and $M_{\xi\xi}$, $M_{\xi\zeta}$, $M_{\eta\eta}$, . . . , are defined in a manner similar to that given in Eq. (12c). Note that all cross-derivative terms have been treated explicitly, and that $\boldsymbol{U}^n$ appearing in those terms can be replaced by $\boldsymbol{U}^n+\Delta\boldsymbol{U}^n$.

The convection terms in Eq. (12) can be upwind differenced by using flux-vector splitting. For example,

$$\left(\frac{\partial}{\partial \xi}\hat{U}^{n+1}\phi\right)_{i,j,k}=\left[\frac{\partial}{\partial \xi}(\hat{U}^+ +\hat{U}^-)\phi\right]_{i,j,k}$$

$$=\frac{\delta_\xi^b(\hat{U}^+\phi)_{i+1/2,j,k}+\delta_\xi^f(\hat{U}^-\phi)_{i-1/2,j,k}}{\Delta\xi}$$

$$\hat{U}^\pm=(\hat{U}\pm|\hat{U}|)/2 \tag{13}$$

where ϕ can be $\boldsymbol{U}$ or $\Delta\boldsymbol{U}$. The other convection terms can be differenced in a similar manner. Here, it is noted that in the upwind operators [e.g., $\delta_\xi^b(\hat{U}^+\phi)_{i+1/2,j,k}$], all metric coefficients (e.g., $\hat{\xi}_t, \hat{\xi}_x, \hat{\xi}_y, \hat{\xi}_z$ in $\hat{U}$) are evaluated at the cell faces (i.e., $i+1/2, j, k$) and are not upwind differenced since they represent the area of the cell faces (recall $\boldsymbol{A}_\xi=J\nabla\xi=(\hat{\xi}_x\boldsymbol{i}+\hat{\xi}_y\boldsymbol{j}+\hat{\xi}_z\boldsymbol{k})$; only flow variables (i.e., u, v, w, $\boldsymbol{U}$, and $\Delta\boldsymbol{U}$) are upwind differenced. This type of differencing makes finite-difference formulation identical to finite-volume formulation if metric coefficients and $\boldsymbol{J}$ are interpreted as cell face areas and volumes, respectively.

For the diffusion terms, they are all centrally differenced but expressed in terms of one-sided difference operators. For example,

$$\left(\frac{\partial}{\partial \xi}\boldsymbol{A}_{\xi\xi}\frac{\partial}{\partial \xi}\frac{\phi^{n+1}}{\rho^{n+1}}\right)_{i,j,k}=\frac{(\boldsymbol{A}_{\xi\xi})_{i+1/2,j,k}}{\Delta\xi^2}\delta_\xi^f\left(\frac{\phi^{n+1}}{\rho^{n+1}}\right)_{i,j,k}-\frac{(\boldsymbol{A}_{\xi\xi})_{i-1/2,j,k}}{\Delta\xi^2}\delta_\xi^b\left(\frac{\phi^{n+1}}{\rho^{n+1}}\right)_{i,j,k} \tag{14}$$

With all spatial derivatives replaced by difference operators as shown by Eqs. (13) and (14), Eq. (12a) can be written as

$$(\boldsymbol{N}+\boldsymbol{B}^b+\boldsymbol{B}^f)\Delta\boldsymbol{U}^{n+1}=\text{RHS} \tag{15a}$$

where

$$\boldsymbol{N}=J^{n+1}\boldsymbol{I}+\Delta t\boldsymbol{D} \tag{15b}$$

$$\boldsymbol{B}^{b,f}=\Delta t\left[\frac{\delta_\xi^{b,f}\hat{U}^{+,-}}{\Delta\xi}+\frac{\delta_\eta^{b,f}\hat{V}^{+,-}}{\Delta\eta}+\frac{\delta_\zeta^{b,f}\hat{W}^{+,-}}{\Delta\zeta}\pm\frac{(\boldsymbol{A}_{\xi\xi})_{i(-,+)1/2,j,k}}{\Delta\xi^2}\delta_\xi^{b,f}\frac{1}{\rho^{n+1}}\pm\frac{(\boldsymbol{A}_{\eta\eta})_{i,j(-,+)1/2,k}}{\Delta\eta^2}\delta_\eta^{b,f}\frac{1}{\rho^{n+1}}+\frac{(\boldsymbol{A}_{\zeta\zeta})_{i,j,k(-,+)1/2}}{\Delta\zeta^2}\delta_\zeta^{b,f}\frac{1}{\rho^{n+1}}\right]\boldsymbol{I} \tag{15c}$$

Now, approximately factor Eq. (15) according to backward- and forward-difference operators and treat source terms as in Ref. 9 to give

$$\boldsymbol{L}\boldsymbol{N}^{-1}\boldsymbol{U}=\text{RHS},\quad \boldsymbol{L}\boldsymbol{N}+\boldsymbol{B}^b,\quad \boldsymbol{U}=\boldsymbol{N}+\boldsymbol{B}^f \tag{16}$$

which can be split as

$$\boldsymbol{L}\,\Delta\boldsymbol{U}^*=\text{RHS} \tag{17a}$$

$$\boldsymbol{U}\,\Delta\boldsymbol{U}^{n+1}=\boldsymbol{N}\cdot\Delta\boldsymbol{U}^* \tag{17b}$$

Application of the preceding two equations at every interior grid point or cell produces the desired block triangular matrices, one lower and one upper. Here, it is noted that in the absence of source terms (i.e., $\boldsymbol{D}$ in $\boldsymbol{N}$), each block on the diagonal of the lower- and upper-triangular matrices formed by Eqs. (17a) and (17b) can be diagonalized if the metric coefficients in the implicit operators are evaluated at cell centers instead of cell faces.[3] This procedure was not employed in this study not because there is a source term but rather because that procedure destroys the conservative property of the implicit operator.

Results

As mentioned earlier, the problem selected to test the method presented in this study is a turbulent boundary layer. More specifically, we are interested in computing the steady-state (in the ensemble-averaged sense) turbulent boundary layer past a flat plate with zero pressure gradient. This problem was selected because diffusion terms play an important role, especially in the direction normal to the wall, and its solutions are well known.

For this turbulent boundary-layer problem, air at static pressure of 1.0 atm and static temperature of 373 K flowed past an adiabatic flat plate at a freestream Mach number of 0.6 with zero pressure gradient. The ratio of specific heats for the air was a constant at 1.4. The domain of interest is a rectangular region that is 0.25 m in height measured from the flat plate and 1.0 m in length measured in the streamwise direction from a location where the Reynolds number based on the momentum thickness is 30,000 (the boundary-layer thickness at that location was 0.10 m).

For this problem, the domain was discretized by using 51 equally spaced grid points in the streamwise direction (x direction) and 125 nonequally spaced grid points in the direction normal to the plate (y direction). In the y direction, grid points were clustered towards the plate (where $y = 0$), and grid spacings varied from 6×10^{-7} m at $y = 0$ (corresponding to $y^+ = \rho u_\tau y/\mu = 0.2$) to 0.025 m at $y = 0.25$ m which resulted in 11 grid points in the linear sublayer ($0 \le y^+ \le 3$), 24 grid points in the buffer layer ($3 < y^+ \le 40$), and 75 grid point in the fully turbulent region.

The equations used to model the turbulent boundary-layer flow are the ensemble-averaged conservation equations of mass, momentum (thin-layer Navier-Stokes), and total energy valid for a calorically and thermally perfect gas. The ensemble-averaged conservation equations were closed by the k-ε model of Chen and Patel which was described in the previous section. In this study, the turbulence model lagged behind the conservation equations of mass, momentum, and total energy by one timestep in the solution procedure. Solutions to the conservation equations were obtained by using the F3D code developed by Steger et al.[10] Solutions to the turbulence model were obtained by using the algorithm described in the previous section; the code which embodies this algorithm will be referred to as RAAKE.

Solutions were first obtained to examine the robustness of the algorithm developed by running RAAKE with the diffusion terms treated explicitly and then implicitly. When the diffusion terms were treated explicitly, numerical experiments indicated that for the current test problem stable numerical solutions can only be obtained if the time-step size is less than about 1×10^{-8} s which is comparable to the maximum timestep size permitted by the explicit stability criterion from linearized analysis (i.e., $\alpha\Delta t/\Delta y^2 \le 1/2$, $\alpha = (\mu + \mu_t/\sigma_k)/\rho$; see Eq. (7) and set $a = 0$ because convection is negligible in that direction and set $b = \alpha\Delta t/\Delta y^2$). When the diffusion terms were treated implicitly, numerical experiments indicated that stable numerical solutions can be obtained with a time-step size as large as 1×10^{-4} s which is also the largest timestep size that can be used by the F3D code for the test problem.

With the robustness of the algorithm established, solutions were obtained to assess its accuracy. This was achieved by using the F3D code with RAAKE in which the diffusion terms were treated implicitly. The time-step size used was 1×10^{-5} s. Solutions were obtained for $k^+ = k/(u_\tau)^2$, $\varepsilon^+ = \mu_w\, \varepsilon/\rho_w U_z^4$, and $u^+ = u/u_\tau$ as a function of $y^+ = \rho u_\tau y/\mu$, where $u_\tau = \sqrt{\tau_w \rho_w}$ is the friction velocity, and the subscript w denotes $y = 0$. The solutions obtained for k^+ and ε^+ are shown in Fig. 1, and they compare well with the known behavior of these quantities[11] (i.e., they fall within the band of available experimental data). The solution obtained for u^+ as a function of y^+ is not shown, but is in excellent agreement (less than 0.05% difference) with the solution obtained by using the Baldwin-Lomax model[12] which is known to provide the correct solution for the current test problem.

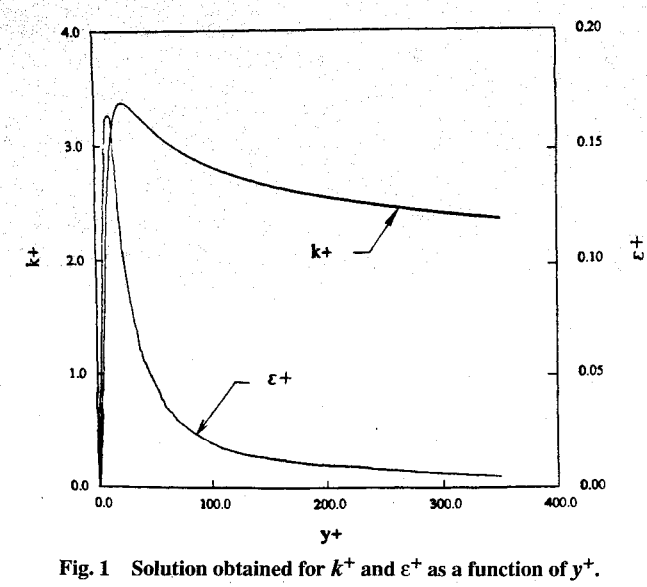

Fig. 1 Solution obtained for k^+ and ε^+ as a function of y^+.

These numerical experiments indicate that the method presented in this study for treating diffusion terms implicitly for the LU algorithm is useful in improving robustness for problems where diffusion terms play an important role.

References

[1]Jameson, A., and Turkel, E., "Implicit Schemes and LU Decompositions," *Mathematics of Computations*, Vol. 37, No. 156, 1981, pp. 385–397.

[2]Steger, J. L., and Warming, R. F., "Flux Vector Splitting of the Inviscid Gasdynamics Equations with Application to Finite-Difference Methods," *Journal of Computational Physics*, Vol. 40, No. 2, 1981, pp. 263–293.

[3]Yoon, S., and Jameson, A., "Lower-Upper Symmetric-Gauss-Seidel Method for the Euler and Navier-Stokes Equations," *AIAA Jounal*, Vol. 26, No. 9, 1988, pp. 1025–1026.

[4]Shuen, J. S., and Yoon, S., "Numerical Study of Chemically Reacting Flows Using a Lower-Upper Symmetric Successive Overrelaxation Scheme," *AIAA Journal*, Vol. 27, No. 12, 1989, pp. 1752–1760.

[5]Yokota, J., "A Diagonally Inverted Lower-Upper Factored Implicit Multigrid Scheme for the Three-Dimensional Navier-Stokes Equations," *AIAA Journal*, Vol. 28, No. 9, 1990, pp. 1642–1649.

[6]Gatlin, B., and Whitfield, D. L., "An Implicit, Upwind, Finite-Volume Method for Solving the Three-Dimensional, Thin-Layer Navier-Stokes Equations," AIAA Paper 87-1149, June 1987.

[7]Chen, H. C., and Patel, V. C., "Near-Wall Turbulence Models for Complex Flows including Separation," *AIAA Journal*, Vol. 26, No. 6, 1988, pp. 641–648.

[8]Wolfshtein, M., "The Velocity and Temperature Distribution in One-Dimensional Flow with Turbulence Augmentation and Pressure Gradient," *International Journal of Heat and Mass Transfer*, Vol. 12, March 1969, pp. 301–318.

[9]Shih, T. I-P., and Chyu, W. J., "Approximate-Factorization with Source Terms," *AIAA Journal*, Vol. 29, No. 10, 1991, pp. 1759–1760.

[10]Steger, J. L., Ying, S. X., and Schiff, L. B., "A Partially Flux-Split Algorithm for Numerical Simulation of Compressible Inviscid and Viscous Flow," Proceedings of the Workshop on Computational Fluid Dynamics, Institute of Nonlinear Sciences, University of California, Davis, CA, 1986.

[11]Patel, V. C., Rodi, W., and Scheuerer, G., "Turbulence Models for Near-Wall and Low Reynolds Number Flows: A Review," *AIAA Journal*, Vol. 23, No. 9, 1985, pp. 1308–1319.

[12]Baldwin, B., and Lomax, H., "Thin Layer Approximation and Algebraic Model for Separated Turbulent Flows," AIAA Paper 78-257, Jan. 1978.

Eigenvalue Sensitivity with Respect to Location of Internal Stiffness and Mass Attachments

B. P. Wang*
University of Texas at Arlington, Arlington, Texas 76019

Introduction

In recent years, sensitivity analysis has attracted great attention in the research community.[1–4] Both static responses and eigenvalue sensitivity with respect to size and shape design variables have been treated. Eigenvalue sensitivity considering shape variables is less developed. Recently, eigenvalue sensitivity for support locations have been reported.[5,6] Specifically, Hon and Chuang[5] applied a material derivative concept in continuum mechanics to derive eigenvalue sensitivity with respect to beam support locations. This result shows that the eigenvalue sensitivity

Received Jan. 31, 1992; presented as Paper 92-2513 at the AIAA/ASME/ASCE/AHS/ASC 33rd Structures, Structural Dynamics, and Materials Conference, Dallas, TX, April 13–15, 1992; revision received Sept. 17, 1992; accepted for publication Sept. 17, 1992.

*Professor, Department of Mechanical and Aerospace Engineering. Member AIAA.